analytical chemistry

Article

pubs.acs.org/ac

HistoMosaic Detecting KRAS G12V Mutation Across Colorectal Cancer Tissue Slices through in Situ PCR

Christopher B. Raub,*,¶ Chen-Chung Lee, Darryl Shibata, Clive Taylor, and Emil Kartalov

Department of Pathology, Keck School of Medicine of the University of Southern California, 2011 Zonal Avenue, Los Angeles, California 90089, United States

Supporting Information

ABSTRACT: We report on HistoMosaic, a novel technique for genetic analysis of formalin-fixed, paraffin-embedded tissue slices. It combines microfluidic compartmentalization, in situ allele-specific PCR, and fluorescence microscopy. The experimental proof of principle was achieved by in situ detection of KRAS G12V mutation in colorectal cancer tissues and is presented herein. HistoMosaic offers the ability to detect mutations over the entire tissue slide simultaneously, rapidly, economically, and without selection bias, while coregistering the genetic information with the preserved morphological information. Thus, HistoMosaic has wide applicability in basic science as a tool to map genetic heterogeneity. It is also a platform to build companion diagnostics for targeted therapies in oncology, to help ensure that the right drug is given to the right patient, thereby saving healthcare resources and improving patient outcomes.

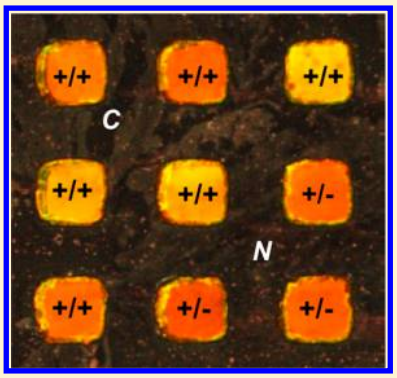

Cancer is a genetically heterogeneous disease that accounted for 8.2 million deaths and 14 million new cases worldwide in 2012.[1] Traditional chemotherapy combats cancer by destroying all rapidly dividing cells, with concomitant harsh side effects. To avoid those effects, targeted therapies[2] disrupt only specific biochemical pathways made dysfunctional by cancer genetic alterations.[3] In 2009, targeted therapies comprised $10.4 billion in sales, or 56% of the oncology drugs market in the US.[4] Cancer cells survive targeted therapy by specific resistance-conferring mutations (mut).[5−7] Even if a targeted therapy completely wipes out the mut− cancer cells, the mut+ subpopulation can survive[8] and repopulate the host tissue, resulting in relapse. Thus, tumor resistance to targeted therapies is a major problem in modern oncology.

Testing for KRAS mutations in colorectal cancer has been recommended since 2009,[9] on a subset of mutations[10] that render anti-EGFR therapies cetuximab and panitumumab ineffective. As a result, in vitro bulk PCR mutation analysis on DNA extracted from the tissue sample is a clinical test offered routinely at major reference laboratories. However, roughly half of the patients that test negative fail the treatment, indicating a deeper problem, e.g., of test sensitivity. Thus, a positive test indicates the need for alternative therapy, such as next generation chemotherapy, while a negative test currently is no guarantee of targeted therapy success. Current requirements on detection sensitivity in terms of abundance of EGFR mutations in nonsmall cell lung cancer[11] and KRAS mutations in CRC[12] are 1% for allele-specific PCR and 10% for Sanger sequencing.

Under ideal conditions, next generation sequencing (NGS),[13,14] laser capture microdissection (LCM),[15] and allele-specific PCR methods[16] approach the 1% requirement. However, NGS is typically costly,[17] and LCM is both costly and time-consuming.[18,19] Further, NGS does not preserve morphologic features of tumor biopsies, and LCM may miss scarce mutations in regions not chosen for extraction. In situ assays such as IHC and traditional FISH have slide-wide coverage and can be related to histomorphometric features, which helps diagnosis and discovery.[20] However, they offer less sensitivity for point mutations than genetic assays.[21] Advanced FISH methods, such as ViewRNA ISH[22] and Stellaris RNA FISH,[23] have sensitivity down to single molecules. They achieve that sensitivity by use of high magnification and numerical aperture, which result in small fields of view that sacrifice coverage to ensure reasonable data acquisition speed. This limits the diagnostic use of these techniques since high coverage is necessary to safeguard against false negatives. The same trade-off limits the clinical application of rolling circle amplification (RCA) techniques that have otherwise demonstrated single-cell sensitivity in in situ mutation detection in frozen and FFPE tissues.[24−27] Thus, no current technique offers all desired features.[28] Therefore, we set off to meet this need.

We reasoned that to maximize coverage and preserve morphological features, the technique must perform in situ PCR on the tissue slices. That approach would also avoid selection bias and ensure simple, fast, and inexpensive processing. The PCR reaction volume would be divided and compartmentalized at the microscale, so that the mutant DNA competes only with the DNA in the same chamber rather than the entire sample. That should boost sensitivity compared to

Received: November 24, 2015
Accepted: January 28, 2016
Published: January 28, 2016

DOI: 10.1021/acs.analchem.5b04460
Anal. Chem. 2016, 88, 2792−2798

bulk PCR methods. We dubbed the resulting technique *HistoMosaic*: *histo* means tissue and *mosaic* refers to the PCR result of each well forming a tile in the mosaic image of the mutation regions in the tissue slice. Its experimental proof of principle is presented herein.

HistoMosaic offers a combination of the morphological selection capability of LCM with the sensitivity of PCR and the coverage of traditional ISH/IHC, while simultaneously being less expensive than NGS. The result is a form of genetic microscopy with PCR-level sensitivity. This new analytical tool has wide applicability in fundamental research, particularly since genetic heterogeneity has emerged as the new paradigm in many fields, of which oncology is just one example. HistoMosaic is also a new diagnostic tool to predict drug resistance at a time when the pharmaceutical industry is under increasing pressure to provide companion diagnostics for expensive therapeutics. As a companion diagnostic, HistoMosaic would ensure that the right drug is given to the right patient, thereby saving healthcare resources and improving patient outcomes.

EXPERIMENTAL SECTION

HistoMosaic Device. The HistoMosaic device (US Patent 8,889,416) consists of three layers. The outer layers are charged glass microscope slides (Diamond, VWR International), one containing a FFPE thin section. A matrixed array of nanoliter-volume wells (ALine Inc.) is positioned onto the tissue of the lower slide and under the top slide. Laser cut well dimensions were 546 μm × 530 μm × 120 μm, with ∼5% error in each dimension. Well volume was estimated to be ∼35 ± 7 nL. Silicone pressure-sensitive adhesive seals the polypropylene wells and connects them to tissue or glass. The wells are loaded with PCR reagents (Reniguard), and the device is placed in a thermocycler (MJR PTC-100, BioRad) for PCR. After an optimal number of cycles, fluorescence signal is detected with a confocal laser scanning microscope (510 Meta, Zeiss) or another instrument. Fluorescence signals are processed in MATLAB (2015a, MathWorks Inc.) to create spatial maps of mutant gene presence (mut+) and absence (mut−, Figure 4d).

Human Colorectal Cancer Tissue. G12V+ and G12V− CRC tissues were provided as 4 μm thick, unstained FFPE sections on charged glass slides (Bristol-Myers-Squibb). Note the G12V+ slide may contain mutation-positive and -negative cells due to tumor genetic heterogeneity. Tissue sections were transverse and contained the luminal surface and underlying connective tissue. FFPE sections were deparaffinized in a graded histosolve/ethanol series, to 100% ethanol, and then dried at 65 °C for 1 h before HistoMosaic assembly.

Assembly and Reagent Loading. HistoMosaic wells were constructed either by photolithography, from SU-8 spun and cured onto the tissue-containing slide, or by laser cutting a PCR film (described below). Care was taken to avoid device contamination with exogenous nucleases or DNA. Final assembly and reagent loading was performed in a sterilized laminar flow hood, using standard PCR contamination avoidance techniques. The laser-cut film was placed directly on the deparaffinized, dried tumor section and pressed with a DNase-free micropipette tip to seal the film to tissue.

Reagent was loaded via a polydimethylsiloxane (PDMS) loading chamber that was sealed to the microscope slide and formed a space 45 × 8 × 0.25 mm above the wells (Figure 1c). PCR reagents were mixed and then loaded into the chamber via one of two 625 μm diameter access holes. To force reagent into

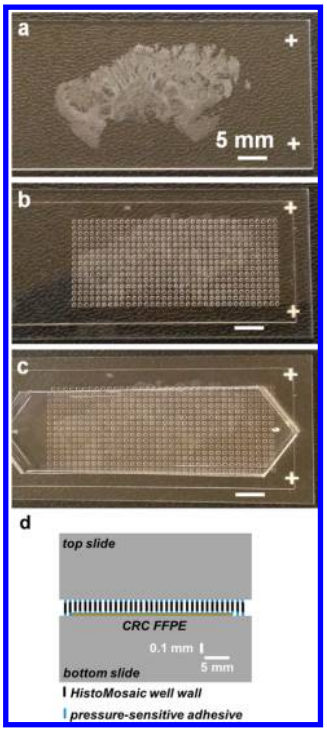

Figure 1. Interfacing of HistoMosaic components. (a) A deparaffinized, formalin-fixed 4 μm section of a human colorectal cancer biopsy on a charged microscope slide. (b) The HistoMosaic well array placed directly on the tissue section, with pressure-sensitive silicone adhesive. Here, 35 × 15 = 525 wells each of 35 ± 7 nL volume provide adequate coverage. (c) The loading chamber aids well filling with PCR reagents by centrifugation at 500*g* and is removable before thermal cycling. Scale bar indicates 5 mm. (d) A schematic of the device profile, with axial and lateral scale, is indicated.

the wells, the slide, wells, and loading chamber with sealed access holes were centrifuged for 1 min at 500*g* (Sorvall Legend T+, Thermo Fisher Scientific). The loading chamber was peeled off, as well as the protective backing on the top side of the well adhesive. A cleaned, blank charged microscope slide was placed on top of the wells aligned with the tissue-containing slide. The completed HistoMosaic device was then placed in a thermal cycler and sealed by lowering the top lid onto a PDMS shim contacting the device over the well region. The lid screw was turned to finger-tightness. The cost to process each HistoMosaic device is about $60 per slide, mostly due to high retail costs of the PCR kit. Equipment needed includes a centrifuge with well-plate holders (Sorval Legend T +, Thermo Fisher Scientific) and a standard thermocycler.

Reagents for Polymerase Chain Reaction. G12V+ and endogenous control targets were amplified by a dual proprietary primer set (Reniguard). The PCR reagent mix contained: master mix (LightCycler 480 Probes Master, Roche), nuclease-free water (Ambion, Life Technologies), primers at 0.5 μM, and probes at 0.1 μM. The G12V mutant probe was 34 bp and conjugated to FAM (494 ex., 518 em.). The constitutive KRAS probe (internal control) was 32 bp and conjugated to HEX (535 ex., 556 em.). Both targets (G12V and constitutive) were less than 70 bp. The thermocycle profile was: 1 × 10 min at 95 °C and then 40 cycles of 1.5 min at 56 °C, 30 s at 95 °C.

Microscopy and Image Analysis. Fluorescence signals from HistoMosaic slides were collected by confocal laser microscopy (Zeiss) and displayed as tiled images covering the

DOI: 10.1021/acs.analchem.5b04460
Anal. Chem. 2016, 88, 2792−2798

entire well array region. The FAM and HEX signals were collected sequentially without repositioning the slide and then digitally coregistered. Both signals were excited and collected through a 10×/NA 0.3 objective (Plan Neofluar, Zeiss). Excitation wavelengths were 488 nm (FAM) and 543 nm (HEX). Emission was collected after filtering by wavelength-selective beam splitters and bandpass filters at 500−550 nm (FAM) and 565−615 nm (HEX). The confocal pinhole was set to 428 μm (FAM) or 480 μm (HEX) to allow fluorescence signal from approximately 60 μm depth. The focal plane was brought to near the center of the 120 μm wells (the signal maximum in the z-direction) to avoid edge effects and tissue autofluorescence. Channel gains were calibrated to utilize the full dynamic range of the channel detector (photomultiplier tube).

Well signal means were detected using an automated image analysis code in MATLAB. Bubbles large enough to exclude the well from analysis (due to lack of reagent) were present in 8 of 144 wells of the HistoMosaic array over G12V+ CRC tissue and 4 of 144 wells of the array over G12V− CRC tissue. Well signals were averaged over a central 210 × 210 (μm × μm) region of each well, placed on each well centroid. Well centroids were determined from automated measurements of wells as objects in binary images created with a threshold of 60 on an 8-bit scale. The binary images were morphologically filtered to isolate each well from background signal. Local background was subtracted from each well mean. The local background was defined as the average signal from four small 70 × 70 (μm × μm) regions in between each well and equidistant from the well edges. Histograms of the noise-subtracted well means were constructed using bins of 10 on an 8-bit scale.

To investigate the role of signal level cutoff values in determining G12V positive (mut+) assignments, the cutoff value was systematically varied while positive wells were counted. The G12V positive cutoff was set at $\mu_{\mathrm{FAM,\ G12\ V-}} + n\mathrm{SD}_{\mathrm{FAM,\ G12\ V-}}$, where $\mu_{\mathrm{FAM,\ G12\ V-}}$ and $\mathrm{SD}_{\mathrm{FAM,\ G12\ V-}}$ are the noise-subtracted well signal mean and standard deviation, respectively, in the FAM channel from the CRC slide section with no KRAS mutation, as determined by Sanger sequencing. The calculations of positive wells were performed with $n = \{1, 2, 3, 4\}$. Wells with bubbles were identified in image analysis and subsequently excluded from signal analysis. Wells that were not defined as G12V positive or containing bubbles were given G12V negative (mut−) assignments.

To aid in histomorphometric comparisons, confocal fluorescence tile-scans of the HistoMosaic wells were coregistered to digital slide scans (Axioscan.Z1, Zeiss) at 20× resolution of serial sections stained with hematoxylin and eosin. Co-registration was automated in MATLAB.

Statistics. To compare distributions of PCR signals over G12V+ versus G12V− tissue, the two-sample Kolmogorov−Smirnov test was performed on noise-subtracted FAM and HEX well means, and significance was set at $\alpha = 0.01$. In this test, the signal distributions are assumed to be continuous, but no shape is assumed. The null hypothesis was that FAM and HEX signals from HistoMosaic wells on the two slides arise from the same continuous distribution. Well numbers analyzed were $n = 129$ for G12V+ and $n = 140$ for G12V− tissue, due to well exclusion criteria described above.

To compare the central tendency of PCR signals over G12V+ versus G12V− tissue, well signal distributions were first assessed for normality using the Anderson-Darling test. Both HEX distributions were approximately normal ($p > 0.05$), but both FAM distributions were non-normal ($p < 0.01$ for both G12V+ and G12V− wells). Independence of wells between the two slides and continuous distributions were assumed. The null hypothesis was that the two population distributions were equal, and the alternative, that the G12V+ signals were greater. Therefore, distributions of noise-subtracted well signal medians were compared using the nonparametric, one-sided Mann−Whitney U test ($\alpha = 0.05$).

RESULTS AND DISCUSSION

Physical Device. The current HistoMosaic device is built by attaching a prefabricated matrix of microwells onto a deparaffinized formalin-fixed, paraffin-embedded (FFPE) tissue slide (Figure 1a,b). The result is loaded with premixed PCR reagents (Figure 1c), sealed with a second glass slide, and placed in a PCR machine for thermocycling. After PCR, the device is scanned in multiple fluorescence colors on a microscope with a mechanized stage. Enzymatic digestion was not performed before PCR.

To rule out interwell leakage in the current procedure, we performed the following experiment. A fluorescence calibration standard was loaded into the device (details in Supplemental Text), with the signal checked before and after 30 thermal cycles, demonstrating no significant change (Supplemental Figure 1).

Assay Optimization. Since the PCR hardware used was not built specifically to work with microscope slides, the achieved thermal ramp rate (1 °C s^{-1}) was significantly slower than typical PCR rates (4−20 °C s^{-1}). Also, the higher surface-to-volume ratio within the microfluidic matrix required a higher content of BSA to prevent PCR inhibition caused by loss of polymerase to nonspecific binding to the walls. These circumstances prompted a reoptimization of the commercial allele-specific assay to fit the needs of the HistoMosaic system. Optimal signal was experimentally achieved for 2.2% (wt/vol) BSA content in the PCR mix (Figure 2a). With that

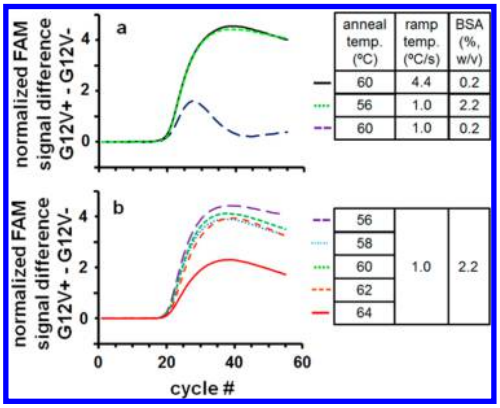

Figure 2. Real-time PCR optimization of HistoMosaic conditions. (a) The normalized FAM (G12V reporter probe) signal difference between separate PCR reactions containing G12V+ target plasmid and G12V− control plasmid was tracked with real-time detection over 55 thermal cycles. Lowering ramp temperature from 4.4 (—) to 1.0 °C/s (— —) produced lower peak signal at a smaller cycle number. An annealing temperature of 56 °C and 2.2% (wt/vol) BSA (- - -) abolished the shift toward lower signal and fewer cycles to peak. (b) At the ramp temperature and BSA levels used in the HistoMosaic assay, the annealing temperature was optimized at 56 °C within the range of 56−64 °C.

DOI: 10.1021/acs.analchem.5b04460
Anal. Chem. 2016, 88, 2792−2798

concentration, the positive control mutant signal was maximized at the annealing temperature of 56 °C, which is at the lower end of the range recommended for the primers (56–64 °C) (Figure 2b).

HistoMosaic Detects G12V in CRC Biopsy Tissue. To obtain the presented data, one G12V+ CRC block and one G12V− CRC block were tested with HistoMosaic. A pair of consecutive sections was prepared from each block. For each pair, one slice was processed by H&E stain to show morphology (Figures 3a and 4a), while the other was tested with HistoMosaic (Figures 3b and 4b). After PCR, each HistoMosaic slice was scanned for FAM and HEX fluorescence emission. For each slice, the resulting two images were combined in false-color pixel-by-pixel, where FAM and HEX fluorescence were indicated with green and red color, respectively. Due to color mixing, the appearance of a yellow pixel would indicate a positive signal in both fluorescence channels. In addition, low-level tissue autofluorescence made morphology features visible. That provided a convenient means of coregistration between HistoMosaic data and H&E scans.

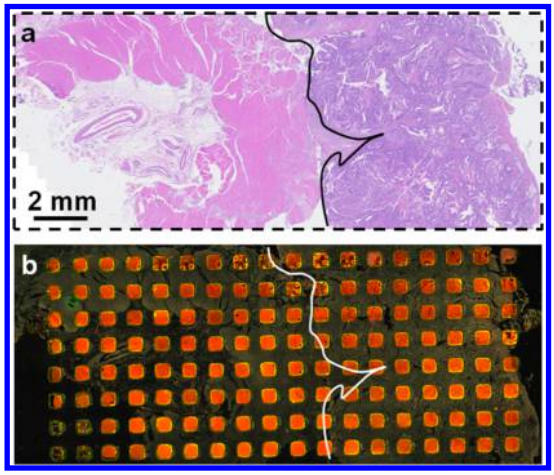

Figure 3. HistoMosaic and H&E serial section comparison for CRC tissue tested G12V− by conventional sequencing. (a) A digital slide scan of a thin section of CRC. (b) A serial, unstained section processed for HistoMosaic and captured as an automated tile scan by confocal laser scanning microscopy. PCR G12V probe (FAM, green) and KRAS probe (HEX, red) fluorescence are limited mostly to within wells. The approximate tumor border is delineated (—). The dual probe signal overlay is combined with autofluorescence background to demonstrate similar morphology of the two serial sections.

Qualitatively, the G12V− slice produced red wells (Figure 3b), while the G12V+ slice produced red and yellow wells (Figure 4b,c). Automated analysis was applied to extract the fluorescence signal in each color from each well (see Experimental Section). A Gaussian fit to the distribution of the FAM signal of the G12V− slice produced a mean and standard deviation which were then used to set up sigma-based cutoffs to call the mut+ or mut− status of wells on the HistoMosaic slides. The results showed that 42%, 23%, and 15% of the wells on the G12V+ slide and 1.4%, 1.4%, and 0.7% of the wells on the G12V− slide were above the 2-, 3-, and 4-sigma cutoff, respectively. These results categorically identify one block as mut+ and suggest the other is mut−, thereby matching the independent results obtained by conventional sequencing on these blocks. This produces an experimental proof of principle for the technique.

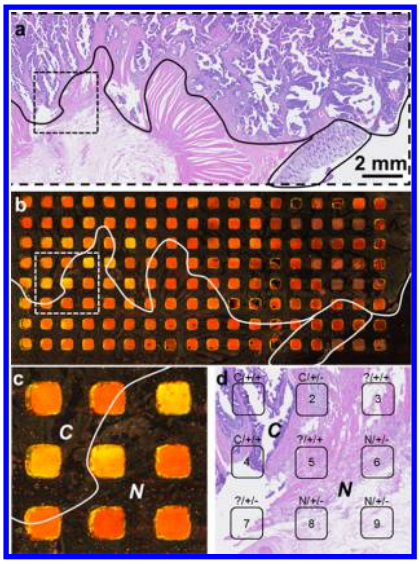

Figure 4. HistoMosaic and H&E serial section comparison for CRC tissue tested G12V+ by conventional sequencing. (a) A digital slide scan of a thin section of CRC. (b) A serial, unstained section processed for HistoMosaic and captured as an automated tile scan by confocal laser scanning microscopy. PCR G12V probe (FAM, green) and KRAS probe (HEX, red) fluorescence are limited mostly to within wells. The approximate tumor border is delineated (—). The dual probe signal overlay is combined with autofluorescence background to demonstrate similar morphology of the two serial sections. Dashed boxes show the locations of (c) and (d). In (d), the symbols above the wells' outlines indicate cancer (C), no cancer (N), no-call (?), KRAS+ or − , and G12V+ or − (well assignments from H&E morphometry and PCR signal statistics). Well numbers 1–9 are referred to in the text.

Statistical Analysis of HistoMosaic Results. The distribution of mutant probe (FAM) noise-subtracted well means from G12V+ tissue was broader and right-skewed compared to G12V− (see Figure 5). The FAM well signal statistics from G12V+ tissue were 65 ± 31 (mean ± SD) and 11–169 (range), while from G12V− tissue, they were 39 ± 14 (mean ± SD) and 0–127 (range). The median FAM probe signal over G12V+ tissue was greater than that over G12V− tissue ($p < 0.0001$, Mann–Whitney U test). FAM probe signal from HistoMosaic wells over G12V+ and G12V− tissue

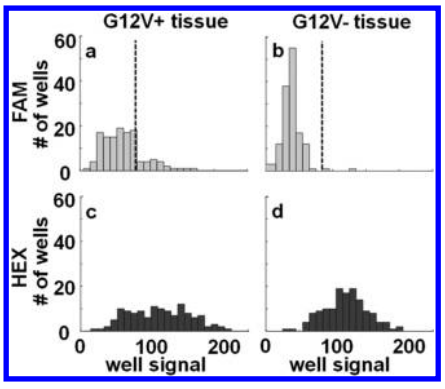

Figure 5. Histograms of HistoMosaic well signals from separate CRC tissue slides. FAM (a, b) and HEX (c, d) signal in tissue that tested positive (a, c), and negative (b, d) for G12V by conventional sequencing. G12V+ cutoff level, $\mu_{FAM,\ G12\ V-} + 2SD_{FAM,\ G12\ V-}$, is indicated (- - -).

DOI: 10.1021/acs.analchem.5b04460
Anal. Chem. 2016, 88, 2792–2798

sections arose from different continuous signal distributions ($p < 0.0001$, Kolmogorov–Smirnov test).

In contrast to the altered mutant probe (FAM) signal, the KRAS probe (HEX) signal was similar between G12V+ and G12V− tissue sections tested with HistoMosaic. The HEX well signal statistics from G12V+ tissue were 118 ± 45 (mean+SD) and 21−221 (range), and from G12V− tissue, they were 119 ± 32 (mean ± SD) and 34−199 (range). The median HEX probe signal over G12V+ tissue was not different than over G12V− tissue ($p = 0.7$, Mann−Whitney U test). HEX probe signal from HistoMosaic wells over G12V+ and G12V− tissue sections arose from similar continuous signal distributions ($p = 0.15$, Kolmogorov−Smirnov test).

Figure 5 shows the histograms of FAM and HEX signals from the wells in Figures 3 and 4. The skewed distribution in FAM is clearly visible for the G12V+ slide. The vertical trace line corresponds to a cutoff calculated from the FAM signal of the G12V− slide, 3-sigma above the mean.

Figure 6 shows the distributions in FAM vs HEX, where each data point corresponds to the noise-subtracted signal from a well. A cutoff of $\bar{x}_{FAM,normal} + 3SD_{FAM,normal}$ (39 + 3 × 14 = 81) was calculated from the control signal distribution, and the respective boxes are drawn to help visualization. These cutoffs determine the mut+ and mut− assignments (See Figure 4d).

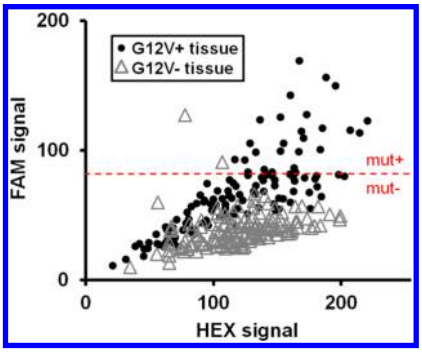

Figure 6. Scatterplot of HistoMosaic well signal for G12V positive (●) and negative (Δ) tissue. G12V+ cutoff level, $\mu_{FAM,\ G12\ V-} + 2SD_{FAM,\ G12\ V-}$, is indicated (- -).

Combinatoric Classification of HistoMosaic Results. HistoMosaic data produces three possibilities in terms of morphology (C, cancer; N, normal tissue; E, empty), two possibilities for the nonmutation-sensitive gene detection (KRAS+ or KRAS−), and two possibilities for mutation allele detection (mut+ or mut−). The total number of possible assignments is 3 × 2 × 2 = 12. The following are examples based on H&E morphometry, staining, and PCR signal quantification, where KRAS/mut status was assigned by comparing well signals to 3-sigma cutoff levels as described above.

Mutation-Negative Normal Tissue (N/+/−). In Figure 4d, the wells in touchphone positions # 6, 8, and 9 contain normal tissue based on the H&E view. The genetic view shows red-weighted wells, indicating KRAS+/mut−.

Mutation-Negative Cancer Tissue (C/+/−). Wells in the upper right corner of Figure 4b contain cancer tissue based on the H&E view. The genetic view shows red wells, indicating KRAS+/mut−.

Mutation-Positive Cancer Tissue (C/+/+). In Figure 4d, the wells in touchphone positions # 1, 2, and 4 contain cancer tissue based on the H&E view. The genetic view shows yellow wells, indicating KRAS+/mut+.

Mutation-Positive Normal Tissue (N/+/+). In Figure 4d, the wells in touchphone positions # 3, 5, and 7 are in normal tissue near the border with cancer, based on the H&E view. The genetic view shows yellow wells, indicating KRAS+/mut+. This is unexpected, because KRAS mutations are unlikely to occur in the stromal cells found in connective tissue. Possible explanations are offered in the discussion below.

These results establish proof of principle for the ability of HistoMosaic to detect KRAS mutations in deparaffinized FFPE tissue sections while preserving tissue morphology. Thus, HistoMosaic can already be used as a tool to provide sample-level yes/no answers in the detection of drug resistant mutations, with higher sensitivity than conventional bulk PCR. That is a consequence of microfluidic compartmentalization, which ensures that mutant DNA competes only with the DNA in the same microfluidic well rather than the DNA of the entire sample. Hence, to detect the mutant, the allele-specific assay only has to overcome a 100× abundance handicap within the well, instead of possibly a 100 000× handicap across the sample. Thus, HistoMosaic already offers superior capability to stratify patients by mutational status, which should avoid some of the false negatives and lead to significant healthcare savings and improved patient outcomes.

In addition to the above capability, HistoMosaic preserves morphological information, which is coregistered with genetic information at the same scale as the matrix unit size. This offers the opportunity to gain high-resolution genetic maps, where the scaling is set by the size of the wells. The smallest HistoMosaic wells we have fabricated photolithographically on tissue so far are 50 μm across, and that is certainly not the limit. As a mammalian cell is typically 10 μm across, it is both feasible and a future goal to extend HistoMosaic to single-cell resolution while retaining the benefits of PCR-based signal gain and PCR assay multiplexing.[29] In the future, the extension of HistoMosaic to the single cell level would require some modifications. Well sizes of approximately 12 pL, with dimensions of ∼10 × 10 × 150 μm, can be fabricated by photolithography with a chromium mask. To avoid adsorption of reagent and/or template, the concentration of BSA will need to be optimized for the higher surface-to-volume ratio of smaller wells. Similarly, the wall thickness of the well mosaic will need to be optimized for the best seal of smaller wells. The DNA template should diffuse upward from the smaller well bottoms in a similar time, since the vertical concentration gradient would not change with decreased lateral well dimensions.

This line of advancement however requires going beyond the statistics of the sample, to understand what happens at the individual well scale. For example, we must understand the few unexpected outcomes, e.g., N/+/+, C/−/−, N/−/−, and E/+/−. N/+/+ means H&E showed normal tissue while HistoMosaic showed KRAS+/mut+. Here, the surprise is the mut+, as KRAS mutations occur in tumor and adjacent normal epithelium[30] but are unlikely to derive from parenchymal cells in connective tissue. A possible explanation is that serial sections are not identical, so the tumor−epithelium−connective tissue boundaries could vary over the distance of ∼1 well, affecting tissue type assignments. Significantly, differences between coregistered autofluorescence and H&E are apparent in Figure 4c,d. If a 1-well wide border zone is added to the tumor to account for serial mismatch, only 3 of 30 mut+ wells

DOI: 10.1021/acs.analchem.5b04460
Anal. Chem. 2016, 88, 2792−2798

would be outside the expected region of mut+. This hypothesis would have to be thoroughly tested by multiple independent methods, e.g., a combination of HistoMosaic, LCM, and advanced FISH.

C/−/− and N/−/− mean H&E showed tissue while HistoMosaic showed KRAS−/mut−. Here, the concern is KRAS−, as all tissue should be KRAS+. One possibility is a systematic failure, e.g., if an air bubble was trapped in the well and prevented its proper filling with PCR reagent. A way to screen such cases is to take an epi-illumination or phase contrast scan as part of the imaging and look for refractive index mismatch. Fortunately, such occurrences are rare based on our experience and may be eliminated by further improvements in the technique. For example, a more sophisticated microfluidic overlay may ensure even more reliable filling than achieved here by centrifugation.

Another possibility is slice-to-slice variation, especially in the cases where the well location appears mostly empty in H&E. That may well mean that even fewer cells, or perhaps no cells at all, are present in the respective well on the HistoMosaic slice. Similarly, the E/+/− case may be the reverse of the same situation, i.e., empty space in H&E but a small number of cells in HistoMosaic leading to a KRAS+ result through PCR amplification.

The typical HistoMosaic wells, with areas of ∼0.25 mm^2, contained some hundreds of cells. The well size could be made smaller with less space in between wells. For example, the smallest HistoMosaic wells we have successfully fabricated on tissue through photolithography were 50 μm across, or 0.0025 mm^2 in area, containing ∼10 cells. Smaller well size would mean greater sensitivity, while thinner walls would offer greater tissue coverage. Smaller wells will also mean greater difficulty in achieving reliable filling by centrifugation, but that can be fixed by making the well walls more hydrophilic (thereby turning an impediment into an advantage) and/or using more sophisticated microfluidic overlay to evacuate the air and thus avoid the current use of dead-end microfluidic priming.[31]

Single-measurement PCR-based techniques are better at detecting small mutations than amplifications, which can be detected with FISH or other techniques.[32] For example, in borderline Her2+ breast cancers, PCR rather than traditional IHC or FISH was more sensitive at detecting the mutation.[32] The single-measurement HistoMosaic assay can be converted to a real-time format by having the hardware acquire fluorescence data from the slide after every PCR cycle. Similar machines already exist, e.g., the Life Tech SOLiD sequencer, and can be modified and repurposed accordingly. Future studies will demonstrate real-time analysis of HistoMosaic and will test the technique on more clinical specimens with validation by laser-capture microdissection plus Sanger sequencing, rather than whole FFPE Sanger sequencing as in the current study.

Real-time HistoMosaic would also allow across-the-slide expression analysis directly from tissue, in a simple, low-cost, and high-throughput format, where the expression information is combined with morphological coregistration. This form of gene expression microscopy would still be limited by PCR multiplexing capacity.[33,34] However, this capability to track a small number of genes simultaneously across the tissue in a high-throughput format and at low cost would be a welcome new tool in a wide range of fields, e.g., developmental biology, oncology, neuroscience, and stem cell research. For example, real-time HistoMosaic would allow quantification of gene copy number alterations, such as amplification of EGFR in breast cancer[35] or cMET in lung cancer.[36,37]

CONCLUSIONS

We have invented, developed, and achieved an experimental proof of principle for HistoMosaic, a novel technique for genetic analysis of FFPE tissue slices by microfluidically compartmentalized in situ PCR. HistoMosaic offers PCR-based sensitivity, high coverage, high speed, low cost, and preserved morphological information. Herein, we have shown that HistoMosaic can detect G12V mutation in CRC, but the technique is applicable to other mutations and cancers in end-point format. HistoMosaic can also be extended to in situ expression analysis by real-time PCR, e.g., for diagnostic use in lung and breast cancer. In the future, HistoMosaic can also be integrated with NGS for even richer genetic information coregistered with morphology. HistoMosaic and its derivative techniques would find impactful applications in fundamental research and drug discovery and as a companion to diagnostics in clinical oncology.

ASSOCIATED CONTENT

Supporting Information

The Supporting Information is available free of charge on the ACS Publications website at DOI: 10.1021/acs.analchem.5b04460.

Test of well seals by tracking fluorescence signal over 30 thermal cycles (Figure S-1). Accompanying text including methods details. (PDF)

AUTHOR INFORMATION

Corresponding Author

*E-mail: raubc@cua.edu. Phone: 213-319-5095. Fax: 213-319-4287.

Present Address

¶C.B.R.: Department of Biomedical Engineering, The Catholic University of America, 620 Michigan Avenue NE, Washington, DC, 20064, USA.

Author Contributions

The manuscript was written through contributions of all authors. All authors have given approval to the final version of the manuscript.

Notes

The authors declare no competing financial interest.

ACKNOWLEDGMENTS

The authors thank the National Institutes of Health (1R21CA174416), the Baxter Family Foundation, and USC Stevens Institute Ideas Empowered Program for their generous funding support. The authors also thank the Caltech Kavli Nanoscience Institute for clean room access and Dr. John Cogswell of Bristol Meyers Squibb for providing tissue samples and PCR reagents.

REFERENCES

(1) Curado, M.; Edwards, B.; Shin, H.; Storm, H.; Ferlay, J.; Heanue, M.; Boyle, P. *IARC Scientific Publication No. 160*; IARC Scientific Publications: Lyon, France, 2007.

(2) Widmer, N.; Bardin, C.; Chatelut, E.; Paci, A.; Beijnen, J.; Leveque, D.; Veal, G.; Astier, A. *Eur. J. Cancer* **2014**, *50*, 2020−2036.

(3) Sawyers, C. *Nature* **2004**, *432*, 294−297.

(4) Aggarwal, S. *Nat. Rev. Drug Discovery* **2010**, *9*, 427−428.

DOI: 10.1021/acs.analchem.5b04460
Anal. Chem. 2016, 88, 2792−2798

(5) Diaz, L. A., Jr.; Williams, R. T.; Wu, J.; Kinde, I.; Hecht, J. R.; Berlin, J.; Allen, B.; Bozic, I.; Reiter, J. G.; Nowak, M. A.; Kinzler, K. W.; Oliner, K. S.; Vogelstein, B. *Nature* **2012**, *486*, 537−540.
(6) Murtaza, M.; Dawson, S. J.; Tsui, D. W.; Gale, D.; Forshew, T.; Piskorz, A. M.; Parkinson, C.; Chin, S. F.; Kingsbury, Z.; Wong, A. S.; Marass, F.; Humphray, S.; Hadfield, J.; Bentley, D.; Chin, T. M.; Brenton, J. D.; Caldas, C.; Rosenfeld, N. *Nature* **2013**, *497*, 108−112.
(7) Aparicio, S.; Caldas, C. *N. Engl. J. Med.* **2013**, *368*, 842−851.
(8) Vogelstein, B.; Papadopoulos, N.; Velculescu, V. E.; Zhou, S.; Diaz, L. A., Jr.; Kinzler, K. W. *Science* **2013**, *339*, 1546−1558.
(9) Allegra, C. J.; Jessup, J. M.; Somerfield, M. R.; Hamilton, S. R.; Hammond, E. H.; Hayes, D. F.; McAllister, P. K.; Morton, R. F.; Schilsky, R. L. *J. Clin. Oncol.* **2009**, *27*, 2091−2096.
(10) Allegra, C. J.; Rumble, R. B.; Schilsky, R. L. *J. Oncol. Pract.* **2015**, *32*, 179−185.
(11) Lindeman, N. I.; Cagle, P. T.; Beasley, M. B.; Chitale, D. A.; Dacic, S.; Giaccone, G.; Jenkins, R. B.; Kwiatkowski, D. J.; Saldivar, J. S.; Squire, J.; Thunnissen, E.; Ladanyi, M. *J. Mol. Diagn.* **2013**, *15*, 415−453.
(12) van Krieken, J. H.; Jung, A.; Kirchner, T.; Carneiro, F.; Seruca, R.; Bosman, F. T.; Quirke, P.; Flejou, J. F.; Plato Hansen, T.; de Hertogh, G.; Jares, P.; Langner, C.; Hoefler, G.; Ligtenberg, M.; Tiniakos, D.; Tejpar, S.; Bevilacqua, G.; Ensari, A. *Virchows Arch.* **2008**, *453*, 417−431.
(13) Mafficini, A.; Amato, E.; Fassan, M.; Simbolo, M.; Antonello, D.; Vicentini, C.; Scardoni, M.; Bersani, S.; Gottardi, M.; Rusev, B.; Malpeli, G.; Corbo, V.; Barbi, S.; Sikora, K. O.; Lawlor, R. T.; Tortora, G.; Scarpa, A. *PLoS One* **2014**, *9*, e104979.
(14) Azuara, D.; Ginesta, M. M.; Gausachs, M.; Rodriguez-Moranta, F.; Fabregat, J.; Busquets, J.; Pelaez, N.; Boadas, J.; Galter, S.; Moreno, V.; Costa, J.; de Oca, J.; Capella, G. *Clin. Chem.* **2012**, *58*, 1332−1341.
(15) Chowdhuri, S. R.; Xi, L.; Pham, T. H.; Hanson, J.; Rodriguez-Canales, J.; Berman, A.; Rajan, A.; Giaccone, G.; Emmert-Buck, M.; Raffeld, M.; Filie, A. C. *Mod. Pathol.* **2012**, *25*, 548−555.
(16) Chang, Y. S.; Er, T. K.; Lu, H. C.; Yeh, K. T.; Chang, J. G. *Clin. Chim. Acta* **2014**, *436*, 169−175.
(17) Salto-Tellez, M.; Gonzalez de Castro, D. *J. Pathol* **2014**, *234*, 5−10.
(18) Boissiere-Michot, F.; Lopez-Crapez, E.; Frugier, H.; Berthe, M. L.; Ho-Pun-Cheung, A.; Assenat, E.; Maudelonde, T.; Lamy, P. J.; Bibeau, F. *Mod. Pathol.* **2012**, *25*, 731−739.
(19) Curran, S.; McKay, J. A.; McLeod, H. L.; Murray, G. I. *Mol. Pathol.* **2000**, *53*, 64−68.
(20) Smith, N. R.; Womack, C. *J. Pathol* **2014**, *232*, 190−198.
(21) Perry, A.; Nobori, T.; Ru, N.; Anderl, K.; Borell, T. J.; Mohapatra, G.; Feuerstein, B. G.; Jenkins, R. B.; Carson, D. *A. J. Neuropathol. Exp. Neurol.* **1997**, *56*, 999−1008.
(22) Laiho, J. E.; Oikarinen, S.; Oikarinen, M.; Larsson, P. G.; Stone, V. M.; Hober, D.; Oberste, S.; Flodstrom-Tullberg, M.; Isola, J.; Hyoty, H. *J. Clin. Virol.* **2015**, *69*, 165−171.
(23) Raj, A.; van den Bogaard, P.; Rifkin, S. A.; van Oudenaarden, A.; Tyagi, S. *Nat. Methods* **2008**, *5*, 877−879.
(24) Mignardi, M.; Mezger, A.; Qian, X.; La Fleur, L.; Botling, J.; Larsson, C.; Nilsson, M. *Nucleic Acids Res.* **2015**, *43*, e151.
(25) Grundberg, I.; Kiflemariam, S.; Mignardi, M.; Imgenberg-Kreuz, J.; Edlund, K.; Micke, P.; Sundstrom, M.; Sjoblom, T.; Botling, J.; Nilsson, M. *Oncotarget* **2013**, *4*, 2407−2418.
(26) Larsson, C.; Grundberg, I.; Soderberg, O.; Nilsson, M. *Nat. Methods* **2010**, *7*, 395−397.
(27) Weibrecht, I.; Lundin, E.; Kiflemariam, S.; Mignardi, M.; Grundberg, I.; Larsson, C.; Koos, B.; Nilsson, M.; Soderberg, O. *Nat. Protoc.* **2013**, *8*, 355−372.
(28) Heuckmann, J. M.; Thomas, R. K. *Ann. Oncol* **2015**, *26*, 1830.
(29) Rajagopal, A.; Scherer, A.; Homyk, A.; Kartalov, E. *Anal. Chem.* **2013**, *85*, 7629−7636.
(30) Zhu, D.; Keohavong, P.; Finkelstein, S. D.; Swalsky, P.; Bakker, A.; Weissfeld, J.; Srivastava, S.; Whiteside, T. L. *Cancer Res.* **1997**, *57*, 2485−2492.
(31) Kartalov, E. P.; Anderson, W. F.; Scherer, A. *J. Nanosci. Nanotechnol.* **2006**, *6*, 2265−2277.
(32) Monego, G.; Arena, V.; Maggiano, N.; Costarelli, L.; Crescenzi, A.; Zelano, G.; Amini, M.; Capelli, A.; Carbone, A. *Scand. J. Clin. Lab. Invest.* **2007**, *67*, 402−412.
(33) Fumagalli, D.; Gavin, P. G.; Taniyama, Y.; Kim, S. I.; Choi, H. J.; Paik, S.; Pogue-Geile, K. L. *BMC Cancer* **2010**, *10*, 101.
(34) Schleifman, E. B.; Tam, R.; Patel, R.; Tsan, A.; Sumiyoshi, T.; Fu, L.; Desai, R.; Schoenbrunner, N.; Myers, T. W.; Bauer, K.; Smith, E.; Raja, R. *PLoS One* **2014**, *9*, e90761.
(35) Bhargava, R.; Gerald, W. L.; Li, A. R.; Pan, Q.; Lal, P.; Ladanyi, M.; Chen, B. *Mod. Pathol.* **2005**, *18*, 1027−1033.
(36) Olivero, M.; Rizzo, M.; Madeddu, R.; Casadio, C.; Pennacchietti, S.; Nicotra, M. R.; Prat, M.; Maggi, G.; Arena, N.; Natali, P. G.; Comoglio, P. M.; Di Renzo, M. F. *Br. J. Cancer* **1996**, *74*, 1862−1868.
(37) Takanami, I.; Tanana, F.; Hashizume, T.; Kikuchi, K.; Yamamoto, Y.; Yamamoto, T.; Kodaira, S. *Oncology* **1996**, *53*, 392−397.

DOI: 10.1021/acs.analchem.5b04460
Anal. Chem. 2016, 88, 2792−2798